Journal of Alloys and Compounds 1026 (2025) 180376

Contents lists available at ScienceDirect

Journal of Alloys and Compounds

journal homepage: www.elsevier.com/locate/jalcom

Mechanisms of ultrasonic vibration-compression treatment on interfacial characteristics and performance enhancement of Ti_p/AZ31 composites

Zhenzhen Gui [a,*], Keying Zhu [a], Pengxi Liu [a], Zhijie Shao [a], Liu Cao [a], Fan Jiang [a], Fan Zhang [a,*], Tao Zhang [b,*]

[a] School of Mechanical and Electrical Engineering, Guangzhou University, Guangzhou Higher Education Mega Center, 230 Wai Huan Xi Road, Guangzhou 510006, China

[b] School of Phycical and Materials Science, Guangzhou University, Guangzhou Higher Education Mega Center, 230 Wai Huan Xi Road, Guangzhou 510006, China

ARTICLE INFO

Keywords:
Ultrasonic Vibration-Compression
Ti_p/AZ31
Interface Evolution
Deformation Coordination

ABSTRACT

In the field of magnesium matrix composites (MMCs), achieving concurrent enhancements in hardness and strength without compromising ductility remains a significant challenge. The utilization of Ti particles as reinforcement phase, which exhibit superior strength and ductility compared to the magnesium (Mg) matrix, facilitates coordinated deformation behavior between Ti particles and the Mg matrix during plastic deformation processes. In this study, ultrasonic vibration-compression (UC) treatment was applied to laser melt injected Ti_p/AZ31 composites. The UC process effectively promoted interfacial phase evolution at Ti/Mg interfaces, establishing robust metallurgical bonding characterized by semi-coherent orientation relationship between Mg and $TiAl_2$ intermetallic compounds at these interfaces. Experimental results demonstrated that under optimized UC parameters (compressive load: 1.5 kN; duration: 10 min), the Ti_p/AZ31-UC composite achieved yield strength (YS) of 239.1 MPa and ultimate tensile strength (UTS) of 284.7 MPa, representing enhancements of 46.2 % and 32.9 % respectively compared to the untreated Ti_p/AZ31 composite, and increases of 281.3 % and 98.9 % relative to the AZ31 matrix, while maintaining a high elongation (EL) of 9.1 %, thereby demonstrating exceptional comprehensive mechanical properties. Concurrently, the Ti_p/AZ31-UC composite microhardness (100.5 HV) exhibited substantial improvements of 123.3 % and 13.7 % compared to the AZ31 matrix (~45 HV) and untreated Ti_p/AZ31 composite (88.4 HV), respectively. These superior comprehensive mechanical properties are predominantly attributed to UC-induced grain refinement and nanoscale interfacial precipitate strengthening.

1. Introduction

Magnesium alloys, recognized as the lightest structural metallic materials, have garnered extensive attention in aerospace, automotive, and defense industries owing to their exceptional combination of low density, high specific strength, high specific stiffness and excellent wear resistance [1–5]. However, the limited mechanical properties and hardness of magnesium and its alloys restrict broader engineering applications [6–8]. In improving the performance of magnesium alloys, significant advancements have been made in plastic processing and surface treatments [9,10]. While plasticity processing methods can improve tensile strength, their effectiveness in microhardness improvement remains limited, often accompanied by drastic reductions in elongation [11–13]. Conventional surface treatments (e.g., micro-arc oxidation, electroless plating) have proven inadequate to effectively improve microhardness and mechanical properties due to weak interfacial adhesion between the coating and the Mg matrix, frequently resulting in premature coating delamination or crack propagation under service conditions [14,15]. Consequently, fabricating particle-reinforced magnesium matrix composites (MMCs) and optimizing the particle-matrix interfacial characteristics have emerged as a scientifically validated strategy for concurrent enhancement of microhardness and mechanical properties [16,17]. Ceramic reinforcement particles such as TiC [18,19], SiC [20,21], and Al_2O_3[22], despite their high hardness, high wear resistance and excellent thermal stability, often induce severe ductility degradation in MMCs due to their intrinsic non-deformability during plastic strain [23,24]. In contrast, metallic reinforcement particles (e.g., Ti, Ni, and Cu), due to their good plasticity and hardness, can enhance the mechanical properties of the magnesium matrix while maintaining its good ductility [25–27].

* Corresponding authors.
E-mail addresses: zhenzhengui@gzhu.edu.cn (Z. Gui), zhf_jd@gzhu.edu.cn (F. Zhang), zhangtao@gzhu.edu.cn (T. Zhang).

https://doi.org/10.1016/j.jallcom.2025.180376
Received 5 March 2025; Received in revised form 8 April 2025; Accepted 10 April 2025
Available online 11 April 2025
0925-8388/© 2025 Elsevier B.V. All rights are reserved, including those for text and data mining, AI training, and similar technologies.

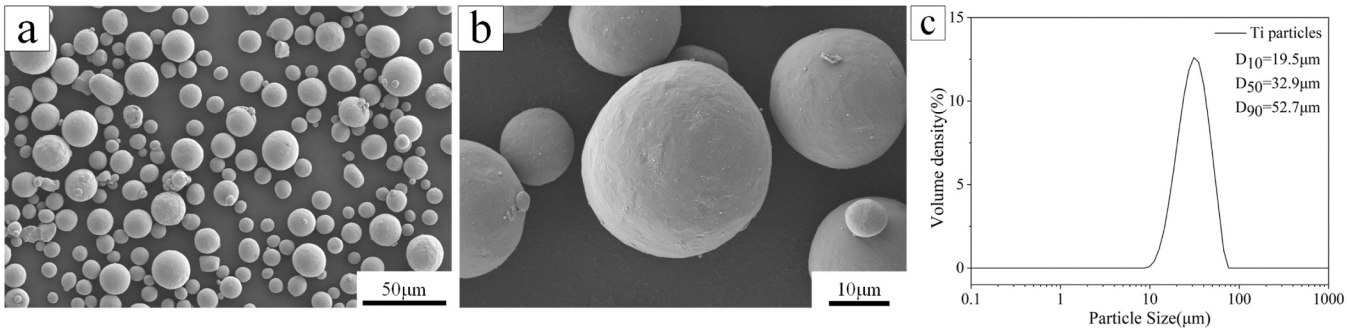


Fig. 1. (a, b) SEM images of Ti particles; (c) Ti particle size distribution.

Further, Ti exhibits particular advantages as an Mg matrix reinforcement that Ti does not react with Mg to form intermetallics, and both share a hexagonal close-packed crystal structure. Meanwhile, Ti's exceptional intrinsic ductility enables active participation in coordinated deformation with the Mg matrix, effectively mitigating the severe ductility loss commonly observed in ceramic-reinforced MMCs [28]. Dinaharan et al. [29] fabricated Ti particle-reinforced MMCs via friction stir processing, achieving a ultimate tensile strength (UTS) of 283 MPa (20.1 % improvement over the 226 MPa matrix) but with reduced elongation (EL) of 9.4 %. Gui et al. [17] developed Ti particle-reinforced Mg-RE (Ti_p/Mg-RE) composites through laser melt injection. While the microhardness of Ti_p/Mg-RE composites increased by 100 % compared to the Mg-RE matrix, the tensile properties deteriorated significantly (UTS: ~160 MPa; EL: ~5 %), primarily due to insufficient interfacial bonding strength between Mg-RE and Ti particles. Ultrasonic vibration-compression (UC), an emerging non-conventional manufacturing technique, has demonstrated remarkable capabilities in microstructural modification and comprehensive mechanical properties enhancement. Xu et al. [30] implemented ultrasonic vibration compression on AZ91 alloy, which induced grain refinement. The treated alloy exhibited a microhardness of 97.2 HV, marking a 37.7 % enhancement over the untreated counterpart. Shao et al. [31] reported that UC treatment on 2A10 aluminum alloy significantly enhanced microhardness from 103 HV to 123 HV, with a 19.42 % improvement. Li et al.[32] applied UC treatment to carbon-doped CoCrNi medium-entropy alloys, achieving UTS and EL of 950 MPa and 36.5 %, respectively, which were 28.3 % and 53.3 % higher than the original state (740 MPa and 23.8 %). Long et al. [33] implemented UC treatment on $AlCoCrFeNi_{2.1}$ high-entropy alloys, realizing simultaneous improvements of 17 % and 54 % in UTS and EL, respectively. Current research predominantly focuses on particle-reinforced metal matrix composites as a primary strategy for material performance enhancement [34,35]. However, single-process approaches exhibit limitations in concurrently enhancing microhardness and mechanical properties. Therefore, exploring the preparation of Ti particle-reinforced AZ31 magnesium matrix composites via laser melt injection followed by ultrasonic vibration-compression is essential for achieving synergistic performance improvements.

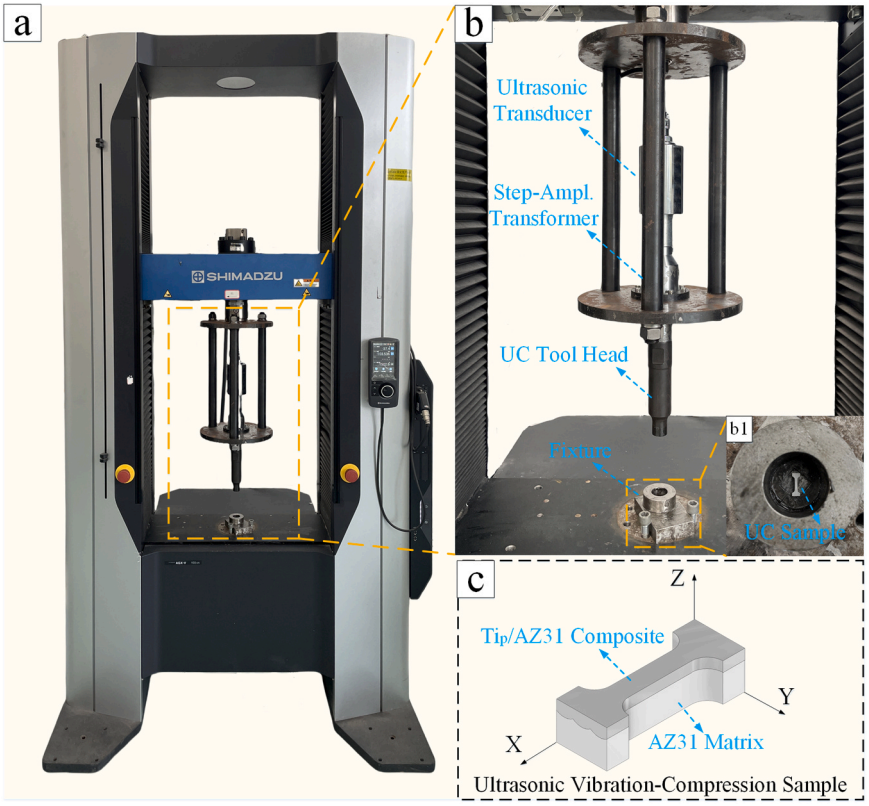


Fig. 2. (a, b) Schematic diagram of UC experimental setup; (c) Sample schematic diagram; (b1) Fixture configuration with sample positioning.

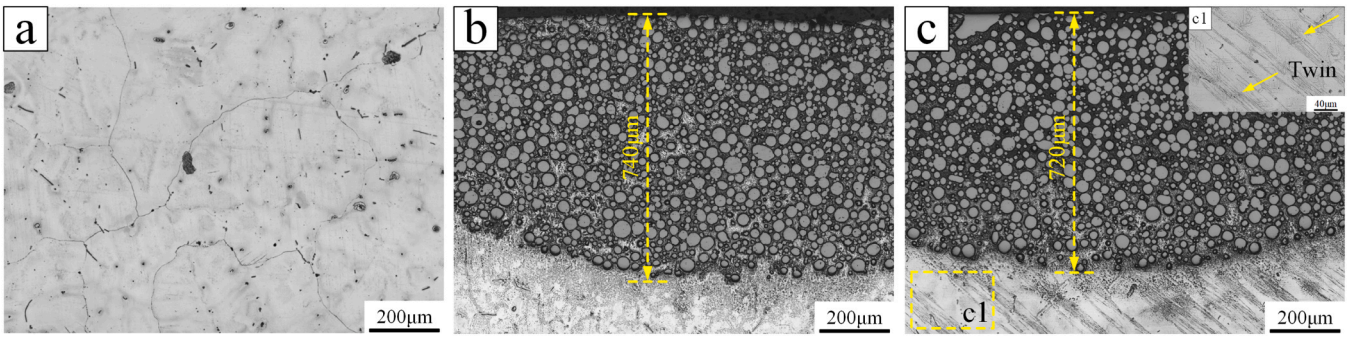


Fig. 3. OM morphology of the cross-sections: (a) As-cast AZ31 matrix; (b) Ti_p/AZ31 composite; (c) Ti_p/AZ31-UC-1.5kN-10min composite.

This study fabricated Ti_p/AZ31 composites via laser melt injection, followed by 20 kHz ultrasonic vibration-compression treatment. The effects of different UC parameters on Ti particle distribution characteristics and Ti/Mg interfacial evolution and interaction mechanism were systematically investigated, with particular emphasis on the analyses of deformation coordination mechanisms and the elucidation on microhardness and mechanical strengthening mechanisms. Experimental results indicate that UC treatment establishes superior metallurgical bonding in Ti_p/AZ31-UC composites, achieving concurrent enhancements in microhardness and tensile strength while maintaining ductility.

2. Materials and methods

2.1. Preparation of composite materials

Commercial as-cast AZ31 alloy was used as the matrix, reinforced with spherical Ti particles (diameter: 15–53 μm). The scanning electron microscopy (SEM) morphology and particle size distribution of Ti particles are presented in Fig. 1. Laser melt injection was performed using an IPG YSL-4000 fiber laser system (spot diameter: 3 mm), with scanning trajectories controlled by a KUKA KR-60HA six-axis robotic arm. To mitigate energy losses caused by Mg alloy's high reflectivity, the laser nozzle was tilted at 5° relative to the matrix surface, with experimental details provided in prior work [17].

2.2. Ultrasonic vibration-compression experiments

UC experiments were conducted at ambient temperature using a custom-designed ultrasonic system, as illustrated in Fig. 2(a, b). The operational principle involves sequential energy conversion: electrical signals are transformed into mechanical vibrations via ultrasonic transducer, amplified to specific amplitudes through stepped amplitude transformer (step-ampl. transformer), and subsequently transmitted to samples as combined vibratory and compressive loads via a UC tool head's indentation stroke. Non-standard tensile samples with dimensions of 11 mm (total length) × 4 mm (width) × 3 mm (thickness) and a 5 mm gauge length were designed for UC processing. Sample positioning within the UC fixture and schematic are provided in Fig. 2 (b1) and 2(c), respectively. UC parameters were configured as follows: vibration frequency 20 kHz, amplitude 20 μm, and the Ti_p/AZ31 composite was loaded at a rate of 50 N/s to the set pressure load. Experiments investigated compressive loads of 1.0 kN and 1.5 kN (~ 60 MPa, i.e., equivalent to the yield strength of as-cast AZ31) with UC treatment durations of 5, 10, and 20 minutes, in order to investigate the effects of different pressure loads and times on the comprehensive performance of the materials. Triplicate samples were prepared per parameter set to ensure statistical reliability. Material designations were assigned as: Ti_p/AZ31 (untreated) and Ti_p/AZ31-UC (UC-treated).

2.3. Properties and performance test of the materials

Pre- and post-UC samples were sectioned, ground, and polished for microstructural characterization using optical microscopy (OM: Leica DM2700M) and scanning electron microscopy (SEM: ZEISS GeminiSEM 460 equipped with BRUKER energy-dispersive X-ray spectroscopy (EDS)). Electron backscatter diffraction (EBSD: FEI Verios 5UC) analysis was conducted on the XOY plane (defined in Fig. 2(c)) for crystallographic orientation mapping to characterize the microstructure

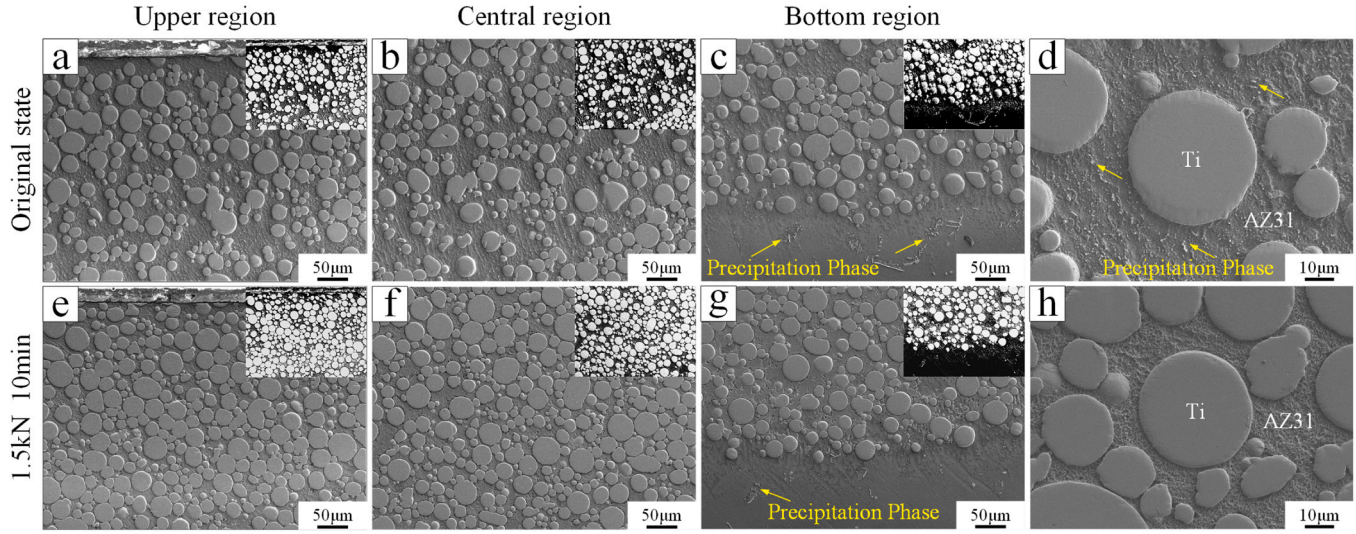


Fig. 4. SEM images of the upper, middle and lower regions of the coating: (a-d) Ti_p/AZ31 composite; (e-h) Ti_p/AZ31-UC-1.5kN-10min composite.

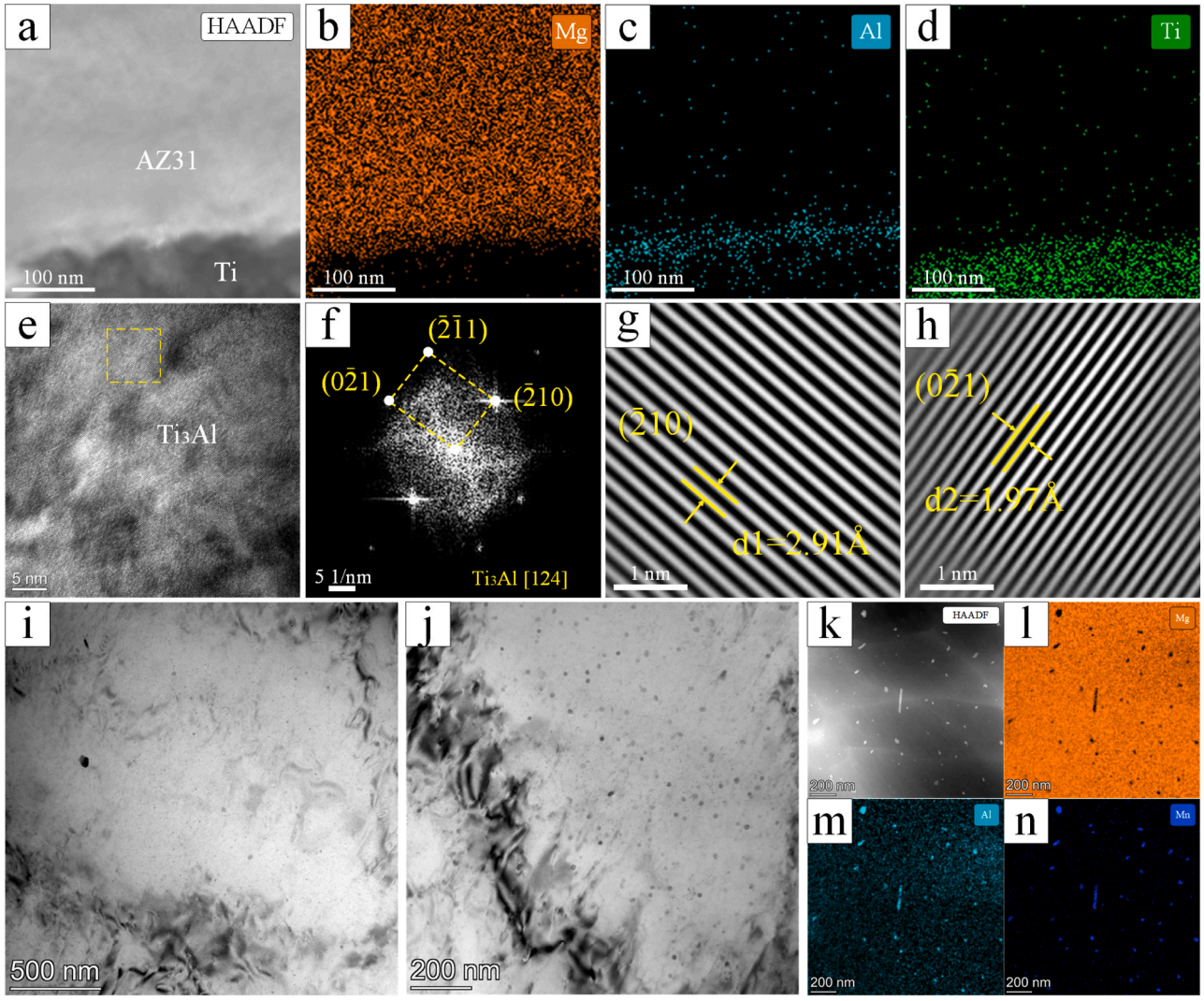


Fig. 5. TEM analysis of Ti_p/AZ31 composite: (a-d) High-angle annular dark-field (HAADF) images and EDS elemental distribution at Ti/Mg interface; (e-h) HRTEM, diffraction spots and IFFT at the interface; (i-j) Bright-field (BF), HAADF image and EDS elemental distribution on the Mg side of Ti_p/AZ31 composite, respectively.

evolution of the samples. Ga-focused ion beam (FIB: Thermo Scientific Scios 2) was employed to prepare transmission electron microscopy (TEM) samples, with subsequent analysis on the interface of the Ti_p/AZ31 composite for elemental mapping performed via TEM (Thermo Fisher Talos F200X, equipped with SuperX G2 EDS). Uniaxial tensile testing was performed using a SHIMADZU AG-XV universal testing machine integrated with a video extensometer at a strain rate of 0.3 mm/min. Tensile specimens were extracted from the Ti_p/AZ31 composite region marked in Fig. 2(c). The excess AZ31 matrix was removed via mechanical grinding, resulting in specimens with a thickness of 1 mm and a gauge length of 5 mm. Mechanical properties, i.e., yield strength (YS), UTS, and EL, were determined as arithmetic means from triplicate tests. Vickers microhardness measurements (Veiyee HV-1000STA) were conducted at 200 g load with 10 s dwell time on the coating cross-sections of the Ti_p/AZ31 composites pre- and post-UC treatment. The testing zones were categorized into four regions: upper coating (top 20 % of the coating thickness, labeled as line "A"), mid-coating (50 % depth, line "B"), fusion line (line "C"), and as-cast AZ31 matrix (150 μm from line C, line "D"). Five replicate measurement tests were performed in each zone to calculate the mean values and standard deviations.

3. Results

3.1. Microstructure of the Ti_p/AZ31 composites

Fig. 3 presents the cross-sectional OM morphologies of the as-cast AZ31 matrix and the Ti_p/AZ31 composites pre- and post-UC treatment. As shown in Fig. 3(a), statistical analysis using the linear intercept method reveals that the as-cast AZ31 matrix exhibits an average grain size of approximately 300 μm. A comparative analysis of Fig. 3(b) and (c) demonstrates that the coating thickness of the Ti_p/AZ31-UC composite (~720 μm) is reduced by 2.7 % compared to the Ti_p/AZ31 composite (~740 μm). Furthermore, the Ti particles in the Ti_p/AZ31-UC composite exhibit a significantly denser distribution. Concurrently, a substantial number of twins are observed in the matrix post-UC treatment, as illustrated in Fig. 3(c1). This twinning phenomenon originates from stress concentration during UC-induced plastic deformation of the Mg matrix. Due to the limited activation of slip systems in the Mg matrix, localized stress concentrations in certain regions induce twin nucleation [36]. Additionally, UC treatment reduces the twin saturation threshold, thereby promoting twin nucleation at lower strains [37].

Fig. 4 presents SEM-based Ti particle distributions in upper, middle, and lower Ti_p/AZ31 composite regions pre- and post-UC treatment. As shown in Fig. 4(a-c, e-g), a variation in the distribution of Ti particles of

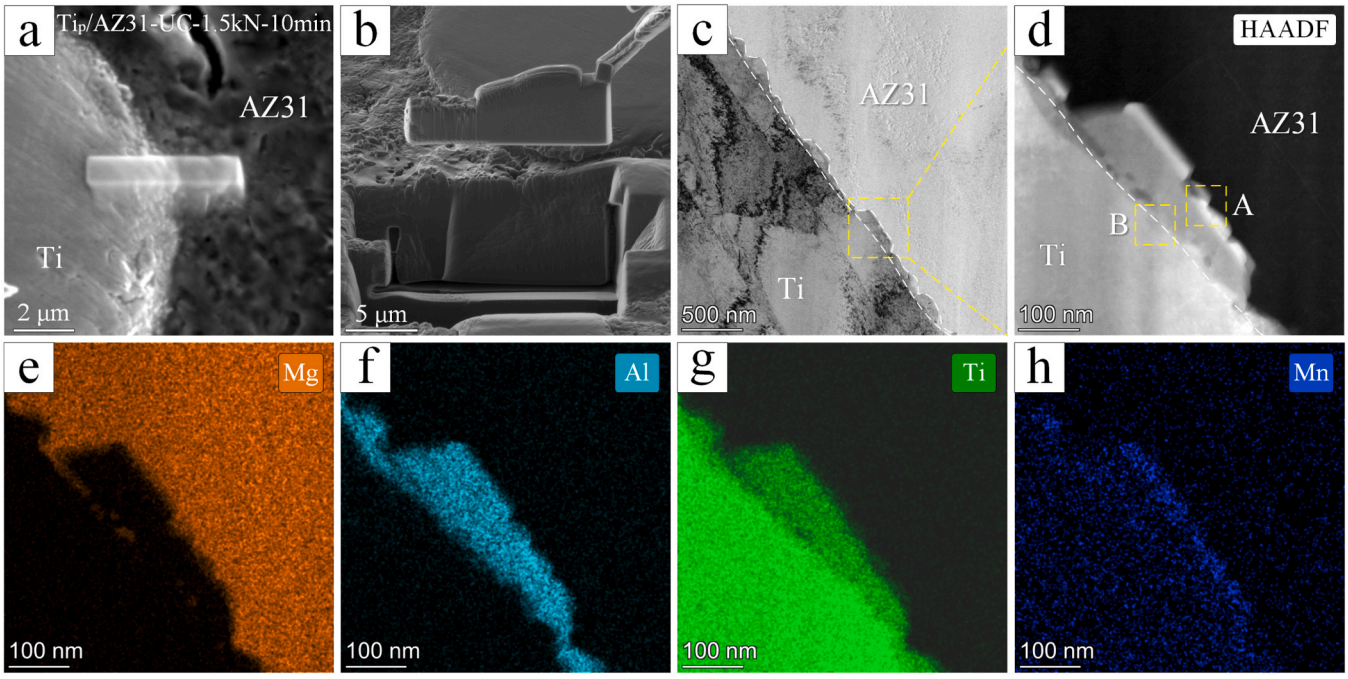


Fig. 6. (a, b) FIB-prepared samples of the interface between Ti particles and the Mg matrix in the Ti_p/AZ31-UC- 1.5kN-10min composite; (c) BF-TEM image; (d) HAADF image; (e-h) EDS elemental maps.

different sizes was observed in the untreated coating, with smaller particles exhibiting a relatively higher density. In contrast, the Ti_p/AZ31-UC composite displays a more homogeneous and denser Ti particle distribution post-UC treatment. This indicates that UC treatment effectively improves Ti particle homogeneity and enhances microstructural densification in the coating. From Fig. 4(c-d, g-h), it is evident that the precipitated phases in both the composite coating and matrix are significantly reduced post-UC treatment compared to the pre-UC state. Binarization analysis reveals that the average area fraction of Ti particles in the Ti_p/AZ31 composite is approximately 60.0 % (see insets in Fig. 4(a-c)), whereas this value increases to 68.7 % in the Ti_p/AZ31-UC composite (insets in Fig. 4(e-g)). Further, regional variations in Ti particle area fraction are observed within the Ti_p/AZ31-UC composite. The upper, middle, and lower regions exhibit Ti area fractions of 75.2 %, 69.1 %, and 61.5 %, respectively, forming a gradient composite coating structure with natural transitions. This gradient structure is attributed to higher ultrasonic energy density at the upper region due to direct tool head contact, generating axial pressure gradients during UC processing.

3.2. Characterization of interfacial bonding

Fig. 5(a) presents the TEM morphology of the Ti_p/AZ31 composite sectioned via FIB, with elemental distributions at the Ti particle/Mg interface shown in Fig. 5(b-d). The results reveal slight Al enrichment at the Ti particle interface, where Al diffuses from the Mg side toward Ti particles, forming Al-Ti intermetallic compounds. As demonstrated in Fig. 5(e-h), high-resolution transmission electron microscopy (HRTEM) phase identification confirms the presence of Al-Ti phases with measured d-spacings d1 = 2.91 Å and d2 = 1.97 Å. Diffraction pattern analysis compared with standard cards identifies these as Ti_3Al phases. Fig. 5(i-j) show TEM microstructure on the Mg side of the Ti_p/AZ31 composite, revealing sparse dislocation distributions. EDS mapping in Fig. 5(k-n) confirms that the precipitated phases in the Mg side of the coating contain Al and Mn elements.

Fig. 6 displays the TEM morphology and elemental distributions at the interface of the Ti_p/AZ31-UC-1.5kN-10min composite sectioned by FIB. From the white dashed region in Fig. 6(c), an Al and Mn-enriched layer with an average thickness of ~75 nm is observed surrounding Ti particles. EDS results indicate enhanced elemental diffusion during UC treatment, generating more abundant and homogeneously distributed Al-Ti and Mn-Ti intermetallic compounds.

To elucidate UC effects on Ti/Mg interfaces, HRTEM phase identification was conducted. As shown in Fig. 7(a) (Region A in Fig. 6(d)) at the interface, diffraction analysis identifies $TiAl_2$, amorphous Mn-Ti phase, and Mg matrix at the interface, suggesting that Al and Mn enrichment layers at the Ti/Mg interface reacted with Ti to form $TiAl_2$ and amorphous Mn-Ti phases. Fig. 7(b) reveals a semi-coherent interface orientation relationship between $TiAl_2$ and Mg: $(\bar{3}11)TiAl_2//(1\bar{1}1)Mg$, $[233]TiAl_2//[231]Mg$. Measured d-spacings are d1 = 2.368 Å and d2 = 1.456 Å for $TiAl_2$, and d1 = 2.459 Å and d2 = 1.913 Å for Mg. Meanwhile, Fig. 7(d) (Region B in Fig. 6(d)) shows Ti phase with identical interplanar spacing of 2.064 Å. Fig. 7(g-o) demonstrate that the Mg side of the Ti_p/AZ31-UC-1.5kN-10min composite exhibits significantly higher dislocation density compared to the pre-UC state (Fig. 5(i,j)). EDS mapping in Fig. 7(i-l) identifies Al and Mn in precipitated phases, with HRTEM diffraction confirming these as Al_8Mn_5 phases. Additionally, a comparative analysis of Fig. 5(k) and 7(i) indicates that the Al_8Mn_5 precipitates transitioned from elongated rod-like and dot-like morphologies to blocky forms post-UC treatment, accompanied by a transformation from clustered to dispersed distribution, as corroborated by the observations in Fig. 4(d) and (h). Owing to the inherent brittleness of Al_8Mn_5 phases, their extensive aggregation may serve as preferential sites for crack initiation during tensile deformation, thereby degrading the strength of the Ti_p/AZ31 composite. In contrast, the homogeneous dispersion of Al_8Mn_5 phases post-UC impedes crack propagation, thereby contributing to enhanced mechanical properties.

3.3. Mechanical properties

Fig. 8 presents the tensile stress-strain curves of the Ti_p/AZ31 and Ti_p/AZ31-UC composites. As shown in Fig. 8(a, b) and Table 1, the YS and UTS of the as-prepared Ti_p/AZ31 composite were 163.5 MPa and 214.2 MPa, respectively, prior to UC treatment. After UC treatment, the mechanical properties of the Ti_p/AZ31-UC composite were significantly

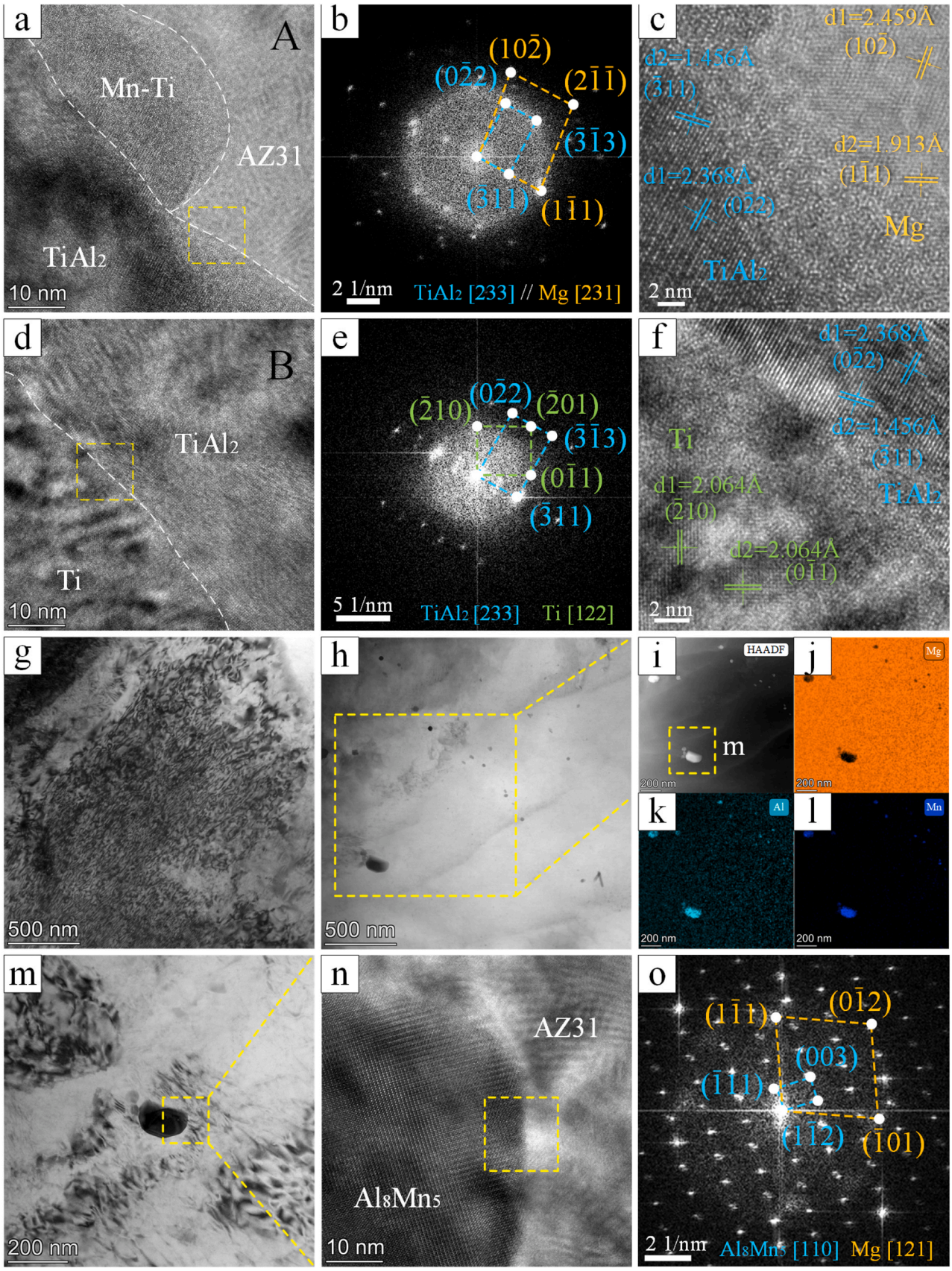


Fig. 7. (a-c, d-f) HRTEM images, diffraction spots, and FFT patterns corresponding to regions A and B in Fig. 5(d); (g-l) BF-TEM image, HAADF image, and EDS elemental distribution maps of the Mg side in the Ti_p/AZ31-UC-1.5kN-10min composite; (m-o) BF-TEM image, HRTEM, and diffraction spots of Figure (i).

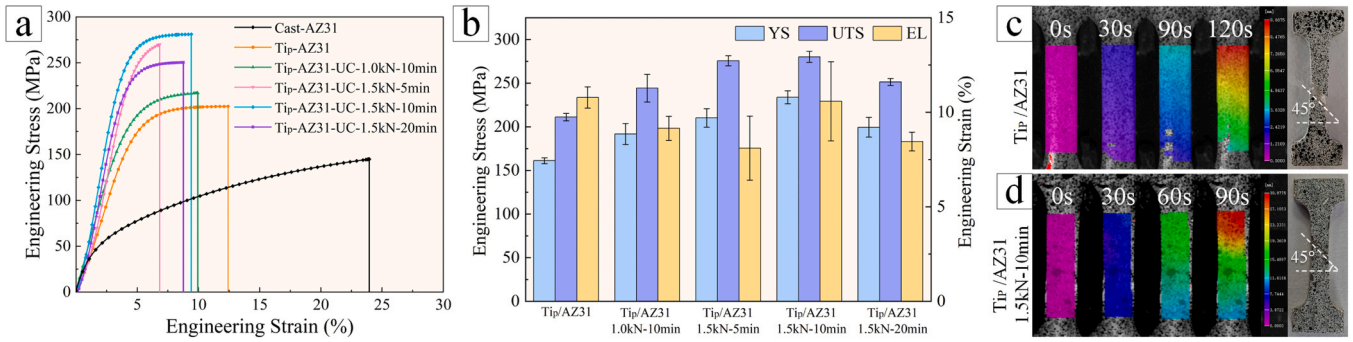


Fig. 8. (a) Engineering stress-strain curves; (b) Tensile properties pre- and post-UC treatment; (c, d) Strain distribution evolution and macroscale fracture surface images.

Table 1
Tensile properties of Ti_p/AZ31 and Ti_p/AZ31-UC composites.

Samples	YS / MPa	UTS / MPa	EL / %
As-Cast AZ31	62.7 ± 4.1	143.1 ± 3.8	23.2 ± 2.6
Ti_p/AZ31	163.5 ± 3.4	214.2 ± 4.3	11.2 ± 0.6
Ti_p/AZ31–1.0 kN−10min	183.2 ± 12.1	233.1 ± 15.7	9.6 ± 0.6
Ti_p/AZ31–1.5 kN−5min	202.7 ± 10.6	271.6 ± 5.7	6.9 ± 1.6
Ti_p/AZ31–1.5 kN−10min	239.1 ± 7.4	284.7 ± 6.3	9.1 ± 2.1
Ti_p/AZ31–1.5 kN−20min	191.5 ± 11.3	254.2 ± 3.9	8.1 ± 0.5

improved. The Ti_p/AZ31-UC-1.5kN-10min composite exhibited optimal performance, with YS and UTS reaching 239.1 MPa and 284.7 MPa, respectively, which were 46.2 % and 32.9 % higher than those of the Ti_p/AZ31 composite, and 281.3 % and 98.9 % higher than those of the as-cast AZ31 matrix, respectively, while maintaining a relatively high EL (9.1 %). The strain evolution of the Ti_p/AZ31 and Ti_p/AZ31-UC composites during tensile deformation was monitored using a video extensometer. The strain distributions along the loading direction are illustrated in Figs. 8(c) and 8(d), respectively. For the Ti_p/AZ31 composite, stress concentration occurred at approximately 90 s during plastic deformation. Subsequent stress accumulation led to preferential microcrack formation and propagation within this region, culminating in fracture at about 120 s. In contrast, the Ti_p/AZ31-UC-1.5kN-10min composite fractured at about 90 s. Fractographic analysis revealed that both untreated and UC-treated Ti_p/AZ31 composites exhibited shear failure along 45° relative to the loading direction. Generally, normal fracture at 90° to the loading direction is indicative of brittle fracture, whereas shear fracture at 45° to the loading direction corresponds to plastic shear fracture[38]. The angular relationship between fracture orientation and loading direction thus confirms the plastic shear characteristics of the Ti_p/AZ31 composite.

To further investigate the tensile strength and ductility mechanisms of Ti_p/AZ31 composites pre- and post-UC treatment, fracture surface characteristics were examined via SEM. As illustrated in Fig. 9(a-c), the fracture behavior of as-cast AZ31 matrix is dominated by transgranular fracture with minor cleavage features. The fracture surface exhibits smooth and parallel cleavage steps, accompanied by localized shallow dimples and tear ridges. Fig. 9(d-f) and (g-i) display the fracture morphologies of Ti_p/AZ31 and Ti_p/AZ31-UC-1.5kN-10min composites, respectively. Microcracks were observed at Ti/Mg interfaces in the fracture of Ti_p/AZ31 composite, whereas the fracture of Ti_p/AZ31-UC composite exhibited Mg matrix partially or fully encapsulating Ti particles, with extensive dimple formation resulting from pronounced plastic deformation. This mechanical behavior originates from the following mechanisms: (i) In the UC-treated coating, the Mg matrix preferentially undergoes plastic deformation during tensile loading, forming characteristic dimples; (ii) Concurrently, the established semi-coherent interfacial orientation relationship between $TiAl_2$ and Mg facilitates efficient load transfer across the interface, enabling stress transmission from the Mg side to Ti particles; (iii) The high-strength and ductile Ti particles effectively share applied loads through elastic deformation, achieving coordinated deformation with the interfacial structure. Notably, some Ti particles undergo coordinated deformation, transitioning from elastic to plastic deformation until fracture occurs, as evidenced in Fig. 9(j-i); (iv) Furthermore, the UC process optimizes Ti particle distribution, achieving a more homogeneous and denser distribution. The synergistic interaction between interfacial load transfer and reinforced Ti particle deformation results in extensive dimple formation within the Mg matrix of Ti_p/AZ31-UC fracture surfaces, significantly enhancing strength while maintaining high elongation. EDS line scan analysis was performed across fractured Ti particles in the tensile fracture surface of the Ti_p/AZ31-UC-1.5kN-10min composite. As shown in Fig. 9(l), significant Al and Mn elemental enrichment was detected surrounding the Ti particles. This observation aligns with the TEM interfacial characterization results in Fig. 7, where the Al and Mn-enriched zones at Ti/Mg interfaces correspond to the formation of deformation-transferable $TiAl_2$ phases and amorphous Mn-Ti phases that enable coordinated deformation. During tensile deformation, the Mg matrix initially undergoes plastic deformation, while the semi-coherent $TiAl_2$ phase formed at the Ti/Mg interface facilitates load transfer from the Mg side to the Ti particles. As deformation progresses, the grains within the Ti particles deform elastically in coordination with the Mg matrix. When the localized stress exceeds the critical resolved shear stress of Ti grains, the Ti particles undergo localized plastic deformation, ultimately leading to the fracture of the Ti particles. In summary, the UC treatment enhances the comprehensive mechanical properties of the Ti_p/AZ31-UC composite by promoting a more homogeneous and denser distribution of Ti particles and establishing metallurgically robust Ti/Mg interfaces.

Fig. 10(a-f) depict the microhardness gradient trends of the Ti_p/AZ31 composite pre- and post-UC. Fig. 10(a, d) illustrates the microhardness gradients from the coating surface to the matrix in Ti_p/AZ31 composites pre- and post-UC treatment. Under optimal UC parameters (1.5 kN load, 10 min duration), the microhardness at zone A increased to 100.5 HV, representing enhancements of 123.3 % and 13.7 % over the as-cast AZ31 matrix (~45 HV) and untreated Ti_p/AZ31 composite (88.4 HV), respectively. The microhardness values at zones B and C increased from 73.8 HV and 56.5 HV to 88.6 HV and 68.1 HV, respectively. This hardening phenomenon primarily originates from the gradient distribution of high-hardness Ti particles from the coating surface to the matrix, coupled with the denser Ti particle distribution post-UC, which intensifies dislocation pinning and impedes slip, thereby inducing pronounced hardening. Microhardness distribution maps (Fig. 10(c, f)) were generated based on the aforementioned measurements to visually elucidate the microhardness evolution.

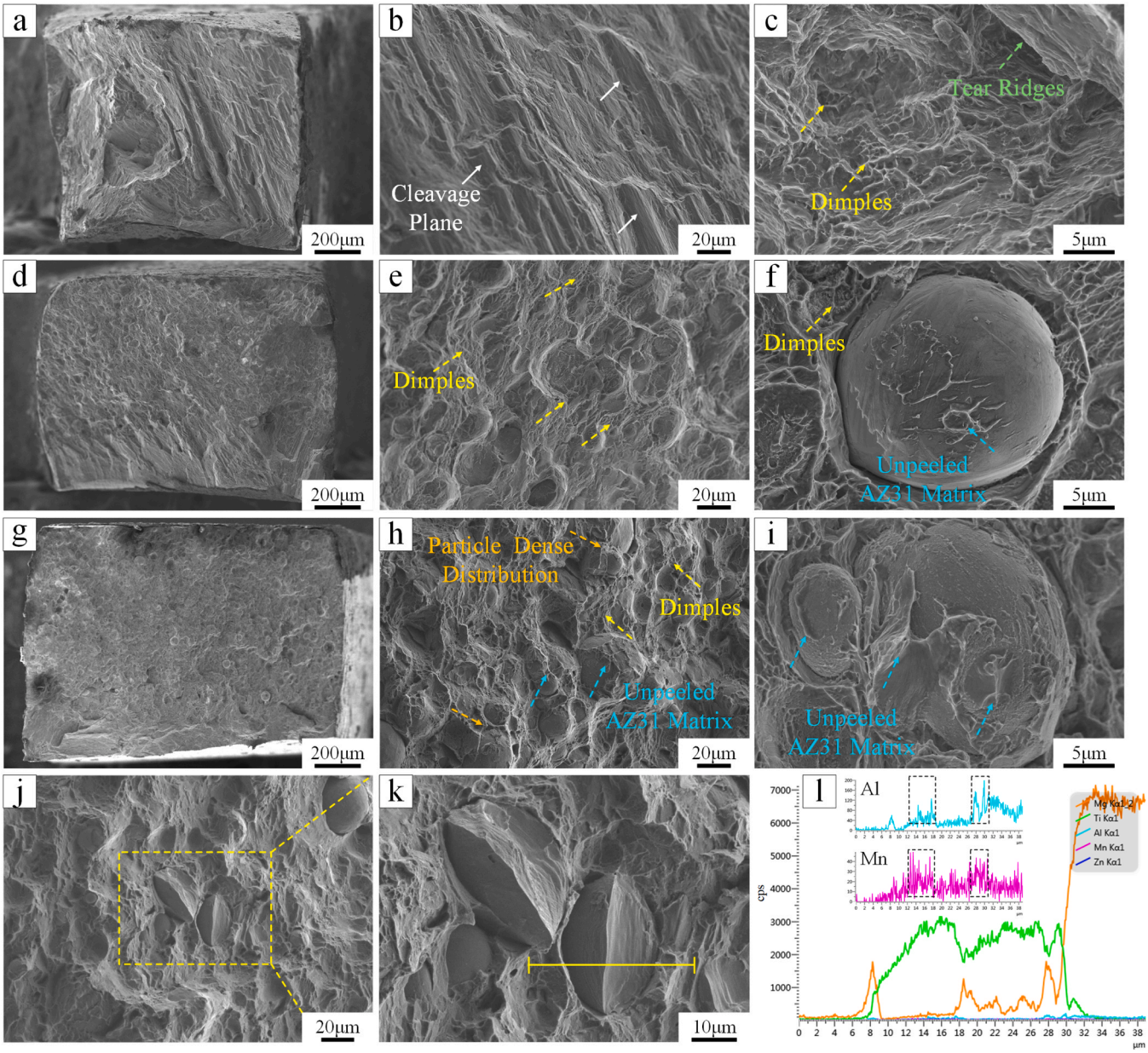


Fig. 9. Fractographic characteristics: (a-c) As-cast AZ31 matrix; (d-f) Ti_p/AZ31 composite; (g-i) Ti_p/AZ31-UC-1.5kN-10min composite; (j-l) EDS line scan analysis of fractured Ti particles in Ti_p/AZ31-UC-1.5kN-10min composite.

4. Discussions

4.1. Analysis of interface between Ti particles and the magnesium matrix

This study demonstrates that UC treatment of Ti_p/AZ31-UC composites achieves exceptional comprehensive mechanical properties through deformation coordination and robust interfacial bonding. As detailed in Section 3.2, an Al-enriched layer was observed at Ti/Mg interfaces. Within the high-temperature Mg molten pool, Al reacted with Ti to form Al-Ti intermetallic compounds, with Gibbs free energy values following the hierarchy: Ti_3Al>TiAl>$TiAl_3$>Ti_2Al_5>$TiAl_2$[39–41]. Prior to UC treatment, Al and Ti reacted to form Ti_3Al phases. The UC process induces atomic migration, enabling the Al and Mn elements dissolved in the Mg side to absorb additional energy and diffuse toward Ti particle interfaces with higher chemical affinity. Consequently, Ti_3Al phases at Ti/Mg interfaces transform into $TiAl_2$ phases with lower Gibbs free energy, forming semi-coherent interfaces with Mg. The transformation reaction is expressed as $Ti_3Al+Al \rightarrow TiAl_2$, and the semi-coherent orientation relationship is recognized as a hallmark of strong interfacial bonding [42,43] Additionally, Mn element deposits at Ti/Mg interfaces, forming layered amorphous Mn-Ti phases.

In summary, during the initial deformation stage of UC, the Mg side of the Ti_p/AZ31-UC composite preferentially deforms due to its lower YS compared to Ti. Concurrently, Al and Mn solutes in the Mg side diffuse toward Ti particle interfaces due to the stronger affinity, driving phase evolution to form $TiAl_2$ and amorphous Mn-Ti interphases. These interfacial phases enhance metallurgical bonding in the Ti_p/AZ31-UC composite, facilitating efficient load transfer from the Mg side to Ti particles. Furthermore, UC treatment homogenizes Ti particle distribution. As deformation proceeds, stress concentration at Ti/Mg interfaces intensifies. Owing to the high strength and ductility of Ti, Ti particles undergo coordinated deformation with the Mg matrix upon reaching critical stress thresholds, alleviating stress concentration and homogenizing strain distribution.

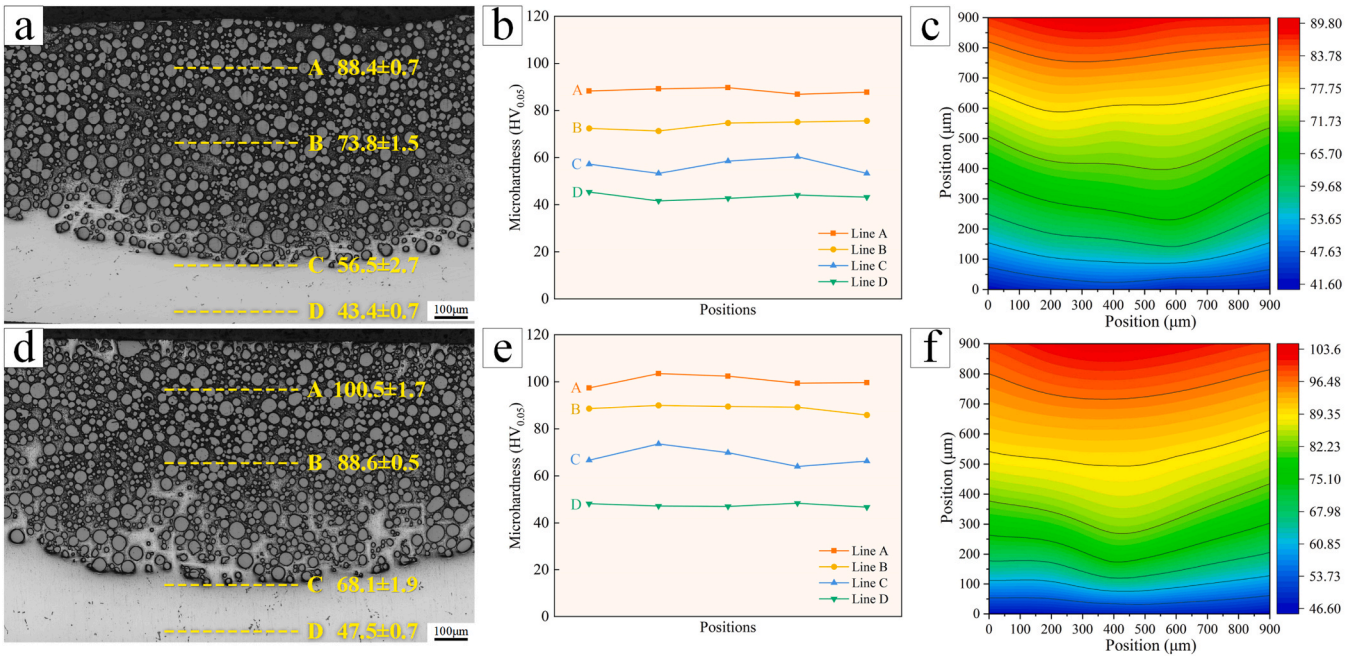


Fig. 10. Microhardness testing positions, measurement results, and distribution maps: (a-c) Ti_p/AZ31 composite; (d-f) Ti_p/AZ31-UC-1.5kN-10min composite.

4.2. Strengthening mechanisms

Kernel average misorientation (KAM) maps shown in Fig. 11(a, f) reveal higher local misorientation around Ti particles prior to UC treatment, whereas post-UC, the misorientation near Ti/Mg interfaces diminishes. This indicates that Ti particles and the Mg matrix undergo coordinated deformation during UC treatment to relieve stress concentration, resulting in reduced KAM values at Ti particles interfaces post-UC treatment. Grain type distributions are shown in Fig. 11(e, j), where blue, yellow, and red colors denote recrystallized, substructured, and deformed grains, respectively. Insets in Fig. 11(e1, j1) provide quantitative grain type statistics. It can be observed from the figures that UC treatment promotes dynamic recrystallization (DRX), increasing the fraction of recrystallized grains from 4.2 % to 5.6 %. Inverse pole figure (IPF) maps and corresponding basal pole figures of Mg and Ti particles pre- and post-UC treatment (Fig. 11(b-c, g-h)) demonstrate that UC treatment alters the crystallographic orientation of the Mg side grains from the original7.75° $< 10\bar{1}0 >$ orientation to148.89° $< \bar{5}173 >$. The basal texture intensities of Mg (0001) and Ti (0001) decrease from 113.14 and 9.94 to 70.99 and 8.47, respectively. The weakened basal texture is attributed to a more homogeneous and denser distribution of Ti particles and grain boundary obstruction of dislocation motion post-UC, which induces dislocation pile-ups and stimulates DRX nucleation. Consequently, the grain orientations in the UC-treated Ti_p/AZ31-UC composite become more randomized. Randomly oriented grains enhance coordinated deformation, preserving ductility in the composite coating [44]. Meanwhile, as observed in Fig. 11(d, d1, i, i1), the average grain size of the Mg matrix grains around the Ti particles decreases significantly from ~5.7 μm to ~1.2 μm post-UC treatment.

The enhancement of mechanical properties through UC treatment can be primarily attributed to three key mechanisms: (i) The UC process induces plastic deformation that stimulates DRX nucleation, significantly refining grain structure; (ii) UC promotes the formation of $TiAl_2$ phases with semi-coherent interfaces to Mg and amorphous Mn-Ti interphases at Ti/Mg interfaces, which synergistically enhance load transfer efficiency during tensile deformation; (iii) UC treatment eliminates fine Ti particle clustering, achieving a homogeneous and dense distribution. These well-distributed Ti particles effectively impede dislocation movement while inducing high-density dislocation networks at particle-matrix interfaces. Concurrently, dislocation pile-ups at grain boundaries form complex tangles that substantially obstruct plastic flow. In conclusion, UC treatment effectively optimizes the mechanical properties of Ti_p/AZ31-UC composites.

The improved tensile strength of the Ti_p/AZ31 composite prepared by laser melt injection, followed by ultrasonic vibration-compression originates from the grain refinement and robust metallurgical bonding at Ti/Mg interfaces. Thus, the strengthening mechanisms of the Ti_p/AZ31 composite pre- and post-UC can be categorized as: (i) Grain refinement strengthening$\Delta\sigma_{H-P}$, (ii) Load transfer strengthening$\Delta\sigma_{Load}$, (iii) Thermal mismatch strengthening$\Delta\sigma_{CTE}$, and (iv) Orowan strengthening$\Delta\sigma_{Orowan}$.

During UC-assisted plastic deformation following laser melt injection of Ti particles, Mg grains in the coating are significantly refined via the dynamic Hall-Petch effect [45]. The contribution of grain refinement to YS enhancement of the composite can be quantified using the Hall-Petch Eq. (1)[46]:

$$\Delta\sigma_{H-P} = K(d_c^{-1/2} - d_m^{-1/2}) \quad (1)$$

where K = 0.13 MPa•$m^{1/2}$ is the Hall-Petch coefficient of AZ31, and d_c and d_m are the average grain sizes of the Ti_p/AZ31 composite and the as-cast AZ31 matrix, respectively. Based on the data obtained from the previous analysis, the YS of the Ti_p/AZ31 composite $\Delta\sigma_{H-P}$ pre- and post-UC was calculated to be 46.9 MPa and 111.2 MPa, respectively. When tensile load is applied to the Ti_p/AZ31 composite, the shear stress is transferred from the Mg side to the interior of the Ti particles. The load transfer strengthening contribution can be calculated using Eq. (2)[47]:

$$\Delta\sigma_{Load} = 0.5V_p\sigma_m \quad (2)$$

where σ_m is the YS of the AZ31 matrix, and V_p is the volume fraction of Ti particles in the coating. Accordingly, the YS of the Ti_p/AZ31 composite $\Delta\sigma_{Load}$ pre- and post-UC treatment was calculated to be 18.8 MPa and 21.6 MPa, respectively. The contribution of thermal mismatch to the increase in YS can be can be quantified via Eq. (3)[48]:

$$\Delta\sigma_{CTE} = \sqrt{3}\alpha G_m b\sqrt{\frac{12V_p\Delta T\Delta C}{(1-V_p)bd_p}} \quad (3)$$

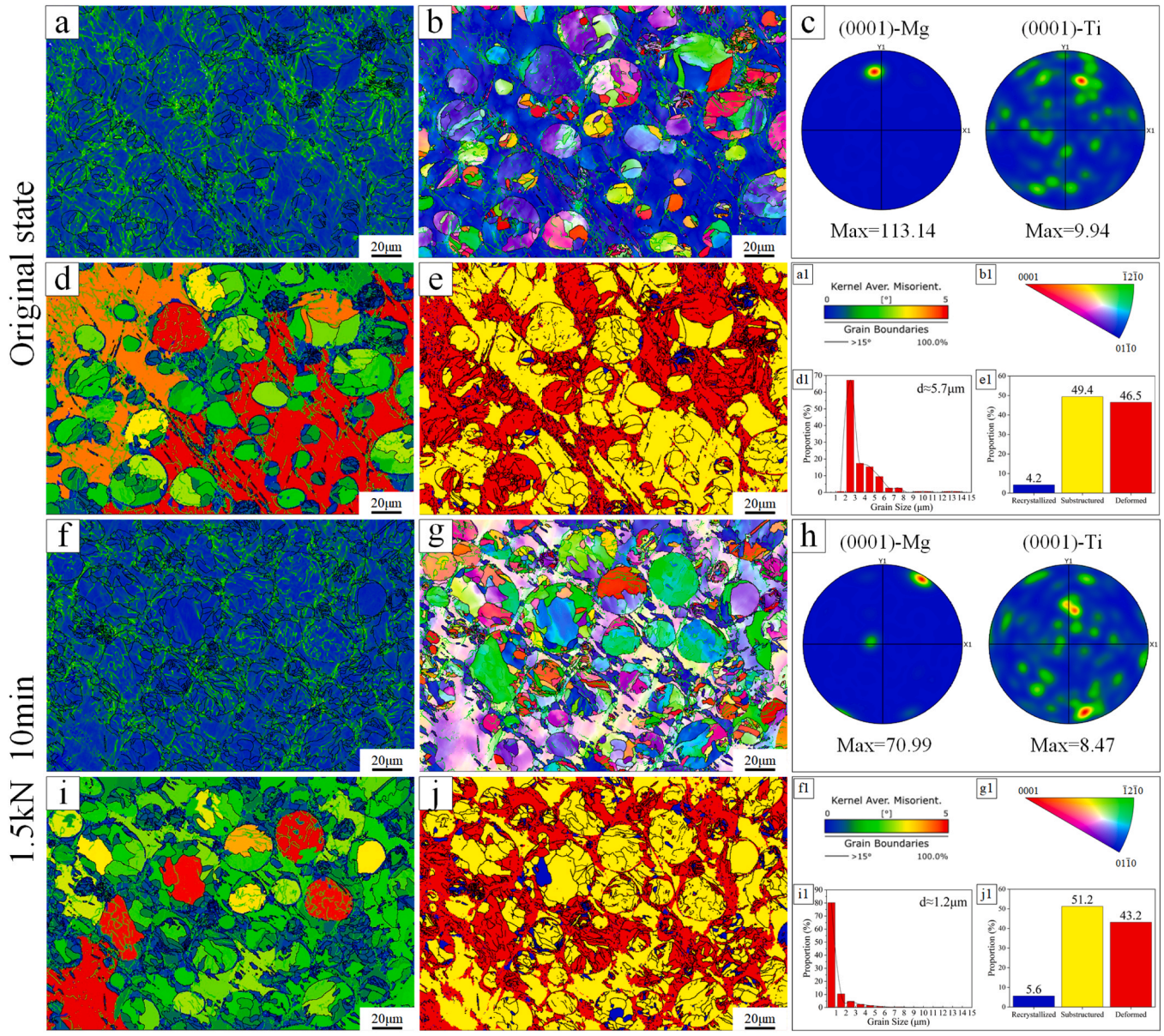


Fig. 11. EBSD analysis of Ti_p/AZ31 composite fractures: (a-e, f-j) KAM maps, IPF maps, pole figures, grain size distributions, and grain type classifications for Ti_p/AZ31 and Ti_p/AZ31-UC-1.5kN-10min; (a1, b1, f1, g1) Legends corresponding to (a, b, f, g), respectively; (d1, i1) Statistical plots of the average grain size of Mg grains in the coating; (e1, j1) Histograms of different grain type distributions.

where $\alpha = 1.25$ is a geometric constant, $G_m = 1.66 \times 10^4$ MPa is the shear modulus of the AZ31 matrix, $b = 3.21 \times 10^{-10}$ m is the Burgers vector, ΔT is the change in temperature, and ΔC is the difference in the thermal expansion coefficients between Ti particles and the AZ31 matrix, and d_p is the average diameter of Ti particles. The calculated YS of the Ti_p/AZ31 composite $\Delta\sigma_{CTE}$ pre- and post-UC treatment was 42.9 MPa and 51.8 MPa, respectively. In the Ti_p/AZ31 composite, homogeneously dispersed Ti particles obstruct dislocation motion through the Orowan mechanism. The YS enhanced by the Orowan mechanism is calculated using Eq. (4)[49]:

$$\Delta\sigma_{\text{Orowan}} = \frac{\varphi G_m b}{d_p}\left(\frac{6V_p}{\pi}\right)^{1/3} \tag{4}$$

where φ is a constant equal to 2. The calculated YS of the Ti_p/AZ31 composite $\Delta\sigma_{Orowan}$ pre- and post-UC treatment was 0.3 MPa and 0.4 MPa, respectively. In summary, the theoretical YS value of the Ti_p/AZ31 composite can be expressed as follows:

$$\Delta\sigma = \sigma_m + \Delta\sigma_{H-P} + \Delta\sigma_{Load} + \Delta\sigma_{CTE} + \Delta\sigma_{\text{Orowan}} \tag{5}$$

The above calculations confirm that grain refinement and thermal mismatch are the dominant strengthening mechanisms. Compared with other strengthening mechanisms, the Orowan mechanism contributes negligibly when the reinforcing particle diameter exceeds 5 μm [50]. Theoretical yield strengths of Ti_p/AZ31 and Ti_p/AZ31-UC-1.5kN-10min composites are 171.6 MPa and 247.3 MPa, respectively. As shown in Fig. 12(a), the discrepancy between theoretical and experimental yield strengths is within ~5 %. Furthermore, Fig. 12(b) compares the UTS and EL of the Ti_p/AZ31-UC composite with other Ti particle-reinforced Mg composites [17,25,51–61], highlighting its superior strength-ductility synergy achieved through laser melt injection coupled with UC treatment.

5. Conclusions

This study systematically investigated the UC treatment applied to

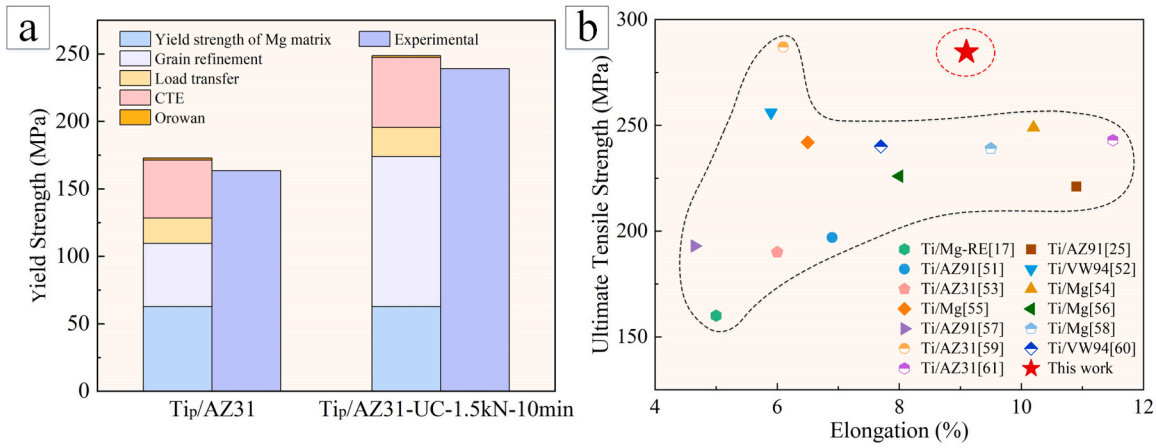


Fig. 12. (a) Theoretical versus experimental yield strengths of Ti_p/AZ31 composite; (b) Comparison of UTS and EL with other representative Ti particle-reinforced Mg composites.

laser melt injected Ti particle-reinforced Ti_p/AZ31 composites. Comprehensive analyses were conducted on the microstructural evolution, interfacial precipitate transformations, microhardness characteristics, and mechanical properties under varying UC conditions, with systematic elucidation of the UC-induced strengthening mechanisms in Ti_p/AZ31-UC composites. The principal conclusions are as follows:

(1) During UC processing, plastic deformation occurred in the Ti_p/AZ31 composite, promoting DRX nucleation. This resulted in significant grain refinement of the Mg grains in the coating, reducing the average grain size from ~5.7 μm to ~1.2 μm. Concurrently, UC treatment optimized Ti particle distribution, achieving a homogeneous and dense distribution. These homogeneously dispersed Ti particles effectively impeded dislocation motion while demonstrating coordinated deformation compatibility with the Mg matrix through sequential elastic and plastic deformation during loading, thereby enhancing load transfer efficiency.

(2) UC treatment induced elemental diffusion of Al and Mn solutes from the Mg side toward Ti particle interfaces. This interfacial redistribution drove phase evolution, forming $TiAl_2$ intermetallic compounds and amorphous Mn-Ti phases at the interfaces. The precipitated $TiAl_2$ phases established semi-coherent orientation relationship $(\bar{3}11)TiAl_2//(1\bar{1}1)Mg$, $[233]TiAl_2//[231]Mg$ with the Mg matrix in AZ31, creating robust metallurgical bonding.

(3) The Ti_p/AZ31-UC-1.5kN-10min composite achieved exceptional comprehensive mechanical properties, with YS, UTS, and EL reaching 239.1 MPa, 284.7 MPa, and 9.1 %, respectively. Compared with the Ti_p/AZ31 composite, the YS and UTS were increased by 46.2 % and 32.9 %, respectively, and compared with the as-cast AZ31 matrix, they were increased by 281.3 % and 98.9 %, respectively. Meanwhile, its microhardness (100.5 HV) exhibited enhancements of 123.3 % and 13.7 % over the AZ31 matrix (~45 HV) and untreated Ti_p/AZ31 composite (88.4 HV). These performance improvements are predominantly attributed to grain refinement strengthening and nanoscale interfacial precipitate strengthening post-UC treatment.

CRediT authorship contribution statement

Gui Zhenzhen: Writing – review & editing, Writing – original draft, Supervision, Project administration, Methodology, Funding acquisition. **Zhu Keying:** Writing – review & editing, Writing – original draft, Funding acquisition, Data curation. **Liu Pengxi:** Investigation, Data curation. **Shao Zhijie:** Investigation, Data curation. **Cao Liu:** Investigation, Formal analysis. **Jiang Fan:** Investigation, Formal analysis. **Zhang Fan:** Writing – review & editing, Supervision, Methodology. **Zhang Tao:** Project administration, Methodology, Funding acquisition, Conceptualization.

Declaration of Competing Interest

The authors declared that they have no conflicts of interest to this work. The manuscript is approved by all authors for publication. I would like to declare on behalf of my co-authors that the work described was original research that has not been published previously, and not under consideration for publication elsewhere, in whole or in part. All the authors listed have approved the manuscript that is enclosed.

Acknowledgements

This work was financially supported by the Guangdong Basic and Applied Basic Research (No. 2022A1515010265, No. 2024A0505040017), the National Natural Science Foundation of China (No. 52371104), and Graduate Innovation Ability Training Program of Guangzhou University (No. JCCX2024-047).

References

[1] J. Liu, H. Jia, S. Wang, P. Ma, J. Xu, M. Zha, H. Wang, Effects of Ca contents on microstructures and mechanical properties of friction stir processed Mg alloys, Mater. Sci. Eng.: A 916 (2024) 147388.
[2] Z. Zhao, T. Zhang, Q. Yang, M. Li, J. Li, Sintering and densification mechanism of SiC particle reinforced AZ91D magnesium matrix composite materials owing binder jetting, Powder Technol. 452 (2025) 120609.
[3] Y. Li, T. Li, J. Wang, Y. Sun, J. Zheng, C. Yang, The effects of in-situ AlN particles on thermal expansion behavior of AZ91 alloy, J. Mater. Res. Technol. 35 (2025) 1776–1786.
[4] M. Subramani, S. Huang, K. Borodianskiy, Effect of WS_2 nanotubes on the mechanical and wear behaviors of AZ31 stir casted magnesium metal matrix composites, J. Compos. Sci. 6 (7) (2022) 182.
[5] S. Wang, M. Zha, H. Jia, Y. Yang, D. Wang, C. Wang, Y. Gao, H. Wang, A review of superplastic magnesium alloys: focusing on alloying strategy, grain structure control and deformation mechanisms, J. Mater. Sci. Technol. 211 (2025) 303–319.
[6] K. Wei, L. Lu, L. Feng, F. Lu, C. Gan, X. Li, Effects of pre-aging on microstructure evolution and deformation mechanisms of hot extruded Mg–6Zn–1Gd–1Er Mg alloys, J. Magnes. Alloy. 11 (1) (2023) 317–328.
[7] J. Song, J. She, D. Chen, F. Pan, Latest research advances on magnesium and magnesium alloys worldwide, J. Magnes. Alloy. 8 (1) (2020) 1–41.
[8] Q. Deng, Y. Wu, Q. Wu, Y. Xue, Y. Zhang, L. Peng, W. Ding, Microstructure evolution and mechanical properties of a high-strength Mg-10Gd-3Y-1Zn-0.4Zr alloy fabricated by laser powder bed fusion, Addit. Manuf. 49 (2022) 102517.
[9] Z. Zhang, J. Zhang, J. Wang, Z. Li, J. Xie, S. Liu, K. Guan, R. Wu, Toward the development of Mg alloys with simultaneously improved strength and ductility by refining grain size via the deformation process, Int. J. Miner. Metall. Mater. 28 (2021) 30–45.
[10] K. Nakazawa, T. Ohashi, S. Saiki, S. Kikuchi, Local oxynitriding of AZ31 magnesium alloy by atmospheric-pressure plasma treatment at room temperature, J. Magnes. Alloy. 10 (7) (2022) 1878–1886.

[11] Z. Zhang, J. Zhang, J. Xie, S. Liu, Y. He, K. Guan, R. Wu, Developing a low-alloyed fine-grained Mg alloy with high strength-ductility based on dislocation evolution and grain boundary segregation, Scr. Mater. 209 (2022) 114414.

[12] B. Che, L. Lu, J. Zhang, J. Zhang, M. Ma, L. Wang, F. Qi, Effects of cryogenic treatment on microstructure and mechanical properties of AZ31 magnesium alloy rolled at different paths, Mater. Sci. Eng. A 832 (2022) 142475.

[13] W. Liu, X. Hu, X. Wang, K. Wu, M. Zheng, Evolution of microstructure, texture and mechanical properties of SiC/AZ31 nanocomposite during hot rolling process, Mater. Des. 93 (2016) 194–202.

[14] J. Lin, W. Chen, Q. Tang, L. Cao, S. Su, Lithium-modified MAO coating enhances corrosion resistance and osteogenic differentiation for pure magnesium, Surf. Interfaces 22 (2021) 100805.

[15] Z. Shao, F. Zhang, Z. Cai, R. Hu, Process and performance of electroless nickel plating on AZ91D magnesium alloy, Anti-Corros. Methods Mater. 64 (2) (2017) 162–169.

[16] I. Dinaharan, S. Zhang, G. Chen, Q. Shi, Titanium particulate reinforced AZ31 magnesium matrix composites with improved ductility prepared using friction stir processing, Mater. Sci. Eng. A 772 (2020) 138793.

[17] Z. Gui, Y. Lu, H. Chen, L. Cao, Z. Kang, G. Wen, D. Liu, Preparation and properties of Ti_p/Mg-RE composites through laser melt injection, Mater. Sci. Eng. B 287 (2023) 116095.

[18] M. Navazani, K. Dehghani, Investigation of microstructure and hardness of Mg/TiC surface composite fabricated by friction stir processing (FSP), Procedia Mater. Sci. 11 (2015) 509–514.

[19] M. Balakrishnan, I. Dinaharan, R. Palanivel, R. Sivaprakasam, Synthesize of AZ31/TiC magnesium matrix composites using friction stir processing, J. Magnes. Alloy. 3 (1) (2015) 76–78.

[20] S. Ganguly, S. Sarkar, A. Mondal, Enhancement of tensile properties of AZ91-Ca-Sb magnesium alloy with SiC nanoparticles additions, Met. Mater. Int. 27 (2021) 3796–3809.

[21] P. Emadi, B. Andilab, K. Borodianskiy, C. Ravindran, Strengthening of Mg-Al-Zn-Mn alloy using SiC/Al nanocomposite extrusion, J. Alloy. Compd. 922 (2022) 166243.

[22] D. Ahmadkhaniha, M. Sohi, A. Salehi, R. Tahavvori, Formations of AZ91/Al_2O_3 nano-composite layer by friction stir processing, J. Magnes. Alloy. 4 (4) (2016) 314–318.

[23] I. Dinaharan, S. Zhang, G. Chen, Q. Shi, Assessment of Ti-6Al-4V particles as a reinforcement for AZ31 magnesium alloy-based composites to boost ductility incorporated through friction stir processing, J. Magnes. Alloy. 10 (4) (2022) 979–992.

[24] S. Huang, M. Subramani, K. Borodianskiy, P. Immanuel, C. Chiang, Effect of equal channel angular pressing on the mechanical properties of homogenized hybrid AZ61 magnesium composites, Mater. Today Commun. 34 (2023) 104974.

[25] D. Pu, S. Wu, H. Yang, X. Chen, J. Li, X. Feng, K. Zheng, F. Pan, Effect of Ti particles on microstructure and mechanical properties of Ti_p/AZ91 composites, J. Mater. Res. Technol. 22 (2023) 1362–1374.

[26] S. Sangral, M. Patel, M. Jayaprakash, Fretting fatigue behavior of magnesium metal matrix composite fabricated through friction stir processing using nickel reinforced particles, J. Fail. Anal. Prev. 22 (3) (2022) 1107–1120.

[27] M. Farghadani, F. Karimzadeh, M. Enayati, N. Naghshehkesh, A. Moghaddam, Fabrication of AZ91D/Cu/Mg_2Cu and AZ91D/Mg_2Cu/$MgCu_2$/MgO in-situ hybrid surface nanocomposites via friction stir processing, Surf. Topogr. Metrol. Prop. 8 (4) (2020) 045002.

[28] H. Yu, Y. Sun, L. Hu, Z. Wan, H. Zhou, Microstructure and properties of mechanically milled AZ61 powders dispersed with submicron/nanometer Ti particulates, Mater. Charact. 127 (2017) 272–278.

[29] I. Dinaharan, S. Zhang, G. Chen, Q. Shi, Titanium particulate reinforced AZ31magnesium matrix composites with improved ductility prepared using friction stirprocessing, Mater. Sci. Eng. 772 (2020) 138793.

[30] Z. Xu, H. Liu, L. Li, C. Sun, X. Tan, B. Chen, Q. Dong, Y. Wu, J. Jiang, J. Ma, Effect of room temperature ultrasonic vibration compression on the microstructure evolution and mechanical properties of AZ91 alloy, Acta Metall. Sin. Engl. Lett. 37 (7) (2024) 1135–1146.

[31] C. Shao, Z. Wang, J. Li, Y. Zhai, J. Lin, R. Bai, Y. Guan, G. Zhao, Investigation of microstructure evolution and mechanical properties of 2A10 aluminum alloy during ultrasonic vibration plastic forming, J. Mater. Res. Technol. 23 (2023) 2467–2478.

[32] Z. Li, X. Long, S. Zhang, H. Deng, M. Zhang, T. Zhang, Ultrasonic provoked network-like intragrain carbide precipitations strengthen and ductilize a C-doped CoCrNi medium entropy alloy, Scr. Mater. 235 (2023) 115633.

[33] X. Long, Z. Li, J. Yan, T. Zhang, Enhanced strength-ductility synergy of an $AlCoCrFeNi_{2.1}$ eutectic high entropy alloy by ultrasonic vibration, J. Mater. Res. Technol. 27 (2023) 4633–4643.

[34] K. Zheng, Y. Lin, J. Cai, C. Lei, Corrosion resistance and tribological properties of laser cladding layer of H13 die steel strengthened by ultrasonic rolling, Chin. J. Mech. Eng. 32 (2022) 137.

[35] C. Chen, Q. Bai, C. Zhao, Q. Li, S. Zhang, Effect of ultrasonic high-frequency micro-forging on the wear resistance of a Fe-base alloy coating deposited by high-speed laser cladding process, Vacuum 221 (2024) 112934.

[36] Q. Shi, K. Deng, K. Nie, W. Zhang, M. Cao, W. Liang, Significant influence of minor SiC_p on microstructure and mechanical properties of pure Mg, J. Mater. Eng. Perform. 29 (2020) 1356–1365.

[37] Q. Cui, X. Liu, W. Wang, S. Tian, V. Rubanik, Jr Rubanik, D. Bahrets, Microstructure and forming mechanism of metals subjected to ultrasonic vibration plastic forming: a mini review, Int. J. Miner. Metall. Mater. 31 (6) (2024) 1322–1332.

[38] X. Ji, Q. An, Y. Xia, R. An, R. Zheng, C. Wang, Maximum shear stress-controlled uniaxial tensile deformation and fracture mechanisms and constitutive relations of Sn-Pb eutectic alloy at cryogenic temperatures, Mater. Sci. Eng. A 819 (2021) 141523.

[39] C. Lin, W. Wu, Y. Han, J. Liu, M. Zhang, Q. Wang, X. Li, Orderly nucleation and competitive growth behaviors of Ti-Al intermetallic compounds in Ti/$TiAl_3$ diffusion couple under high temperature, J. Alloy. Compd. 939 (2023) 168815.

[40] C. Zhang, X. Wang, X. Wang, X. Hu, K. Wu, Fabrication, microstructure and mechanical properties of Mg matrix composites reinforced by high volume fraction of sphere TC4 particles, J. Magnes. Alloy. 4 (4) (2016) 286–294.

[41] U. Kattner, J. Lin, Y. Chang, Thermodynamic assessment and calculation of the Ti-Al system, Metall. Trans. A 23 (1992) 2081–2090.

[42] J. Ye, X. Chen, H. Luo, J. Zhao, J. Li, J. Tan, H. Yang, B. Feng, K. Zheng, F. Pan, Microstructure, mechanical properties and wear resistance of Ti particles reinforced AZ31 magnesium matrix composites, J. Magnes. Alloy. 10 (8) (2022) 2266–2279.

[43] Q. Yuan, G. Zhou, L. Liao, Y. Liu, L. Luo, Interfacial structure in AZ91 alloy composites reinforced by graphene nanosheets, Carbon 127 (2018) 177–186.

[44] S. Xiang, M. Gupta, X. Wang, L. Wang, X. Hu, K. Wu, Enhanced overall strength and ductility of magnesium matrix composites by low content of graphene nanoplatelets, Compos. Part A Appl. Sci. Manuf. 100 (2017) 183–193.

[45] O. Bouaziz, N. Guelton, Modelling of TWIP effect on work-hardening, Mater. Sci. Eng. A 319 (2001) 246–249.

[46] L. Liu, X. Zhou, S. Yu, J. Zhang, X. Lu, X. Shu, Z. Su, Effects of heat treatment on mechanical properties of an extruded Mg-4.3 Gd-3.2 Y-1.2 Zn-0.5 Zr alloy and establishment of its Hall–Petch relation, J. Magnes. Alloy. 10 (2) (2022) 501–512.

[47] H. Yu, H. Zhou, Y. Sun, L. Ren, Z. Wan, L. Hu, Microstructures and mechanical properties of ultrafine-grained Ti/AZ31 magnesium matrix composite prepared by powder metallurgy, Adv. Powder Technol. 29 (12) (2018) 3241–3249.

[48] J. Cui, H. Yang, Y. Zhou, J. Tan, X. Chen, J. Song, G. Huang, K. Zheng, Y. Jin, B. Jiang, Optimizing the microstructures and enhancing the mechanical properties of AZ81 alloy by adding TC4 particles, Mater. Sci. Eng. A 863 (2023) 144518.

[49] L. Chen, J. Xu, H. Choi, M. Pozuelo, X. Ma, S. Bhowmick, J. Yang, S. Mathaudhu, X. Li, Processing and properties of magnesium containing a dense uniform dispersion of nanoparticles, Nature 528 (7583) (2015) 539–543.

[50] Z. Zhang, D. Chen, Consideration of orowan strengthening effect in particulate-reinforced metal matrix nanocomposites: a model for predicting their yield strength, Scr. Mater. 54 (7) (2006) 1321–1326.

[51] X. Ai, G. Quan, Effect of Ti on the mechanical properties and corrosion of cast AZ91 magnesium alloy, Open Mater. Sci. J. 6 (1) (2012) 6–13.

[52] D. Pu, X. Chen, J. Wang, J. Tan, J. Li, H. Yang, B. Feng, K. Zheng, F. Pan, Effect of Ti particles on the LPSO phase and mechanical properties of Ti_p/VW94 composites, J. Mater. Res. Technol. 25 (2023) 3324–3336.

[53] I. Dinaharan, S. Zhang, G. Chen, Q. Shi, Development of titanium particulate reinforced AZ31 magnesium matrix composites via friction stir processing, J. Alloy. Compd. 820 (2020) 153071.

[54] J. Hao, J. Zhang, C. Xu, Y. Zhang, Effects of Ti addition on the formation of LPSO phase and yield asymmetry of Mg-Zn-Y-Mn alloy, Mater. Sci. Eng. A 735 (2018) 99–103.

[55] P. Cheng, Y. Zhao, R. Lu, H. Hou, Effect of the morphology of long-period stacking ordered phase on mechanical properties and corrosion behavior of cast Mg-Zn-Y-Ti alloy, J. Alloy. Compd. 764 (2018) 226–238.

[56] S. Sankaranarayanan, R. Sabat, S. Jayalakshmi, S. Suwas, M. Gupta, Effect of hybridizing micron-sized Ti with nano-sized SiC on the microstructural evolution and mechanical response of Mg-5.6 Ti composite, J. Alloy. Compd. 575 (2013) 207–217.

[57] F. Yao, G. You, L. Wang, Q. Li, S. Zeng, Y. Ming, Design, fabrication, microstructure, and mechanical properties of interlayer-free vacuum diffusion bonding Mg/Ti composites, Vacuum 199 (2022) 110947.

[58] S. Hassan, M. Gupta, Development of ductile magnesium composite materials using titanium as reinforcement, J. Alloy. Compd. 345 (1-2) (2002) 246–251.

[59] J. Ye, J. Li, H. Luo, J. Tan, X. Chen, B. Feng, K. Zheng, F. Pan, Effect of micron-Ti particles on microstructure and mechanical properties of Mg–3Al–1Zn based composites, Mater. Sci. Eng.: A 833 (2022) 142526.

[60] D. Pu, X. Chen, Y. Ding, Y. Sun, B. Feng, K. Zheng, F. Pan, Effect of Ti particles size on the microstructure and mechanical properties of Ti_p/VW94 composites, Mater. Sci. Eng. A 858 (2022) 144140.

[61] P. Gao, S. Han, Y. Zhang, B. Fang, X. Zhang, X. Wang, H. Ding, K. Zheng, F. Pan, Investigation on the interface bonding and reinforcement mechanism of nano Ti/AZ31 magnesium matrix composites, J. Mater. Res. Technol. 30 (2024) 4908–4919.